Baird, A., Kendall, J. M., Fisher, Q. J., & Budge, J. (2018). The role of texture, cracks, and fractures in highly anisotropic shales. *Journal of Geophysical Research: Solid Earth*, *122*(12), 10341–10351. https://doi.org/10.1002/2017JB014710

AGU PUBLICATIONS

JGR

Journal of Geophysical Research: Solid Earth

RESEARCH ARTICLE
10.1002/2017JB014710

Key Points:
- Details of aligned fabric and fractures in shale were inferred using shear wave splitting
- We observe a clear *S* wave triplication due to anisotropy, very rarely observed in field-scale data
- We infer constraints on subhorizontal crack properties which may play an important role in fluid flow

Supporting Information:
- Supporting Information S1
- Data Set S1

Correspondence to:
A. F. Baird,
alan.baird@bristol.ac.uk

Citation:
Baird, A. F., Kendall, J.-M., Fisher, Q. J., & Budge, J. (2017). The role of texture, cracks, and fractures in highly anisotropic shales. *Journal of Geophysical Research: Solid Earth*, *122*, 10,341–10,351. https://doi.org/10.1002/2017JB014710

Received 13 JUL 2017
Accepted 18 NOV 2017
Accepted article online 23 NOV 2017
Published online 26 DEC 2017

The Role of Texture, Cracks, and Fractures in Highly Anisotropic Shales

Alan F. Baird[1], J. Michael Kendall[1], Quentin J. Fisher[2], and Jessica Budge[3]

[1]School of Earth Sciences, University of Bristol, Bristol, UK, [2]School of Earth and Environment, University of Leeds, Leeds, UK, [3]Nexen Energy ULC, Calgary, Alberta, Canada

Abstract Organic shales generally have low permeability unless fractures are present. However, how gas, oil, and water flows into these fractures remains enigmatic. The alignment of clay minerals and the alignment of fractures and cracks are effective means to produce seismic anisotropy. Thus, the detection and characterization of this anisotropy can be used to infer details about lithology, rock fabric, and fracture and crack properties within the subsurface. We present a study characterizing anisotropy using *S* wave splitting from microseismic sources in a highly anisotropic shale. We observe very strong anisotropy (up to 30%) with predominantly VTI (vertical transverse isotropy) symmetry, but with evidence of an HTI (horizontal transverse isotropy) overprint due to a NE striking vertical fracture set parallel to the maximum horizontal compressive stress. We observe clear evidence of a shear wave triplication due to anisotropy, which to our knowledge is one of only a very few observations of such triplications in field-scale data. We use modal proportions of minerals derived from X-ray fluorescence data combined with realistic textures to estimate the contribution of intrinsic anisotropy as well as possible contributions of horizontally aligned cracks. We find that aligned clays can explain much of the observed anisotropy and that any cracks contributing to the vertical transverse isotropy (VTI) must have a low ratio of normal to tangential compliance (Z_N/Z_T), typical of isolated cracks with low hydraulic connectivity. Subhorizontal cracks have also been observed in the reservoir, and we propose that their reactivation during hydraulic fracturing may be an important mechanism to facilitate gas flow.

1. Introduction

Organic-rich shales represent a substantial energy resource; however, due to their fine grain size they typically have low matrix permeabilities and are difficult to produce unless fractures are available to enhance gas flow. Shales also often have strong seismic anisotropy, which can be caused by the preferred alignment of intrinsically anisotropic minerals such as clays (Kendall et al., 2007; Sayers, 2005; Vernik & Nur, 1992) and can also be produced by the presence of aligned cracks or fractures (Crampin, 1984; Hudson, 1980). Thus, the study of anisotropy may be used to infer the interplay between fabric and fractures in shale reservoirs. Here we estimate anisotropy in a shale using *S* wave splitting (SWS) measurements from microseismic data acquired during hydraulic fracture stimulation.

Anisotropy due to horizontally aligned sedimentary fabric will produce an anisotropic system with a vertical axis of symmetry (vertical transverse isotropy, VTI). VTI anisotropy can be fully characterized using the vertical and *P* and *S* velocities (V_{P0} and V_{S0}) combined with the Thomsen (1986) parameters—ε, γ, and δ. These can be used to describe how the *P* wave velocity and the horizontally (*SH*) and vertically (*SV*) polarized *S* wave velocities vary with inclination (Figure 1). The ε and γ parameters describe the fractional difference between the horizontal and vertical velocities of the *P* and *SH* waves, respectively. In shales ε and γ both tend to be positive (i.e., higher horizontal velocities than vertical) and correlate with each other (Horne, 2013; Pervukhina & Rasolofosaon, 2017). The δ parameter is more difficult to describe because its effect depends on its value compared to the ε parameter. A special case, referred to as elliptical anisotropy, occurs when δ equals ε, so named because it produces elliptical *P* wavefronts from a point source and spherical *SV* wavefronts (Figure 1a). Note that the *SH* wavefront is elliptical for all VTI cases. In most shales, however, δ is less than ε (Horne, 2013). This distorts the *P* and *SV* velocity surfaces at oblique angles, producing velocities that are slower and faster, respectively, compared to the elliptical situation, which may result in the *SV* and *SH* wavefronts crossing each other (Figure 1b). In extreme cases, when ε is high and δ is sufficiently low, the *SV* velocity surface will fold

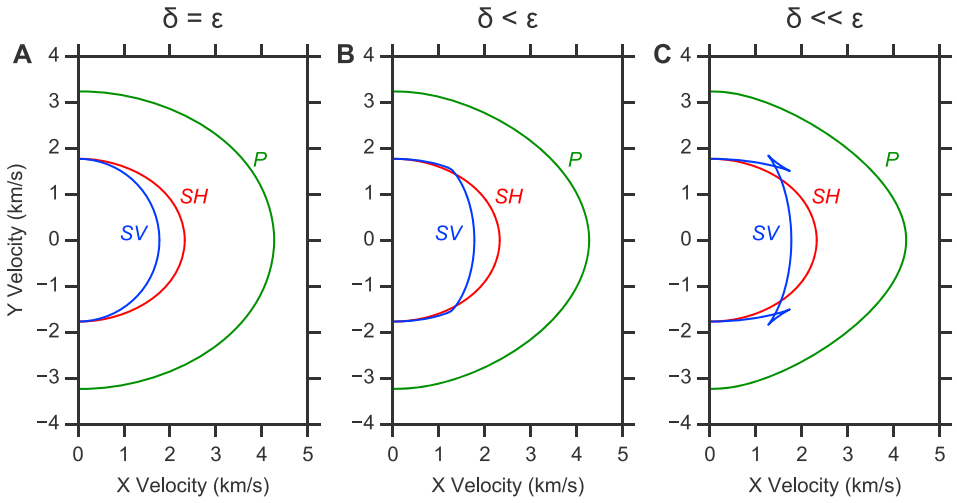

Figure 1. Group velocity surfaces for *P*, *SH*, and *SV* waves in a VTI anisotropic medium with (a) elliptical anisotropy (V_{P0} = 3.235 km/s, V_{S0} = 1.77 km/s, $\varepsilon = \delta = 0.37$, and $\gamma = 0.36$), (b) δ lowered to 0.15 such that the *SV* and *SH* wavefronts cross, and (c) δ further lowered to −0.05 to introduce triplications in the *SV* wavefront.

into itself producing multivalued wavefronts known as triplications, or cusps (Dellinger, 1991; Thomsen & Dellinger, 2003) (Figure 1c). Such triplications have been known about theoretically for some time; however, they are relatively rarely observed in field-scale data.

Another anisotropic parameter useful for analyzing the size of *SV* triplication is σ, defined by Tsvankin and Thomsen (1994) as

$$\sigma = \Gamma_0^2(\varepsilon - \delta), \tag{1}$$

where Γ_0 is the vertical V_P/V_S ratio. Thomsen and Dellinger (2003) showed that the condition for off-axis triplication occurs when σ exceeds a critical value given by

$$\sigma_{\text{crit}} = \frac{2}{3}\left(1 + \delta - \frac{1}{9\Gamma_0^2}\right) \equiv \frac{18 + 18\varepsilon - 2/\Gamma_0^2}{27 + 18/\Gamma_0^2}. \tag{2}$$

Indeed, the ratio $\sigma/\sigma_{\text{crit}}$ is found to be the dominant factor controlling the size of the triplications, even for rocks with different values of ε and Γ_0.

In addition to sedimentary fabric, aligned fractures or cracks can also contribute to the overall anisotropy of a shale reservoir. Their effect will depend on some measure of the strength of the fracture set, usually quantified with a fracture density term (η), the ratio of normal to tangential compliance of the fracture (Z_N/Z_T), and fracture orientation. For example, fracture sets are often steeply dipping or vertical which would produce an anisotropic system with a horizontal symmetry axis (horizontal transverse isotropy, HTI) in the absence of sedimentary fabric. In practice, however, there is usually some sedimentary fabric that the fractures are overprinting producing an orthorhombic symmetry (Baird et al., 2013; Verdon et al., 2009) (i.e., three orthogonal symmetry planes). Alternatively, horizontal fractures, microcracks, or compliant pores may be present that would simply enhance the already existing VTI anisotropy (Allan et al., 2016; Sayers, 2005).

There are many techniques available to estimate anisotropy including the detection of nonhyperbolic moveout velocities (e.g., van der Baan & Kendall, 2002; Tsvankin & Thomsen, 1994), or reflection amplitude variations with azimuth and inclination (e.g., Hall & Kendall, 2003; Lynn & Thomsen, 1990). However, perhaps the simplest indicator of anisotropy is *S* wave splitting. An *S* wave will split into two approximately orthogonally polarized waves traveling at different speeds when it passes through an anisotropic medium. Anisotropy along the raypath can be characterized by measuring the polarization (ψ) of the fast wave and the delay time (δt) between the wave arrivals (typically δt is normalized by path length to be expressed as a percentage *S* wave velocity difference, δV_S). *S* wave splitting is particularly useful when applied to microseismic data recorded using downhole arrays, as microseismic events typically produce strong *S* waves and both the source and receiver are in the rock of interest (Baird et al., 2013; Verdon et al., 2009).

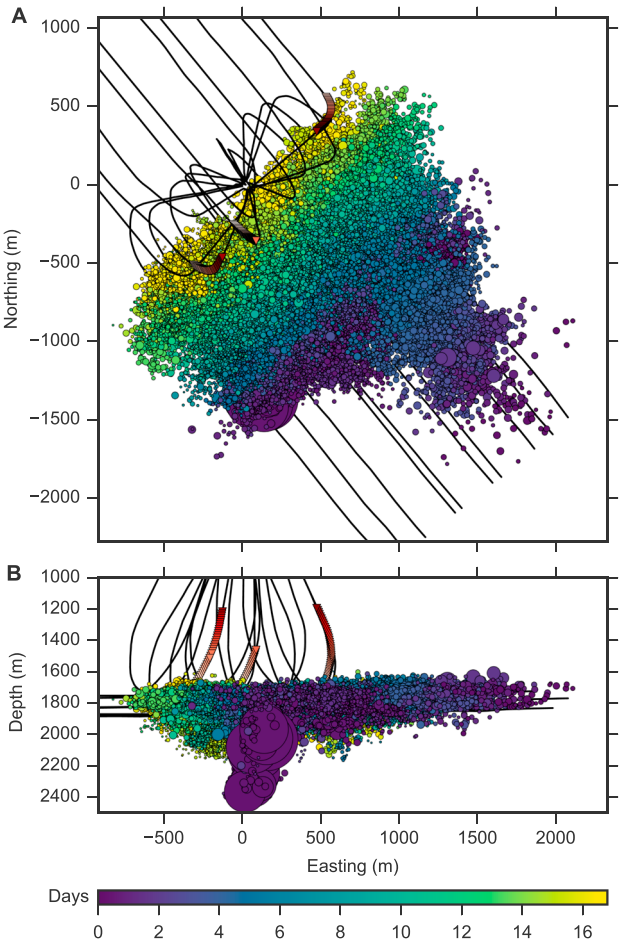

Figure 2. (a) Map view and (b) cross-sectional view of microseismic event locations. Well trajectories are shown as black lines and geophone arrays as red triangles. Events are colored by time after the first event in the data set and the size proportional to the inferred rupture area.

2. Microseismic Data Set

The microseismic data set we consider was acquired during hydraulic fracturing in the Horn River formation in northeastern British Columbia. This is a quartz-rich gas-bearing shale, consisting of three members: the Muskwa, Otter Park, and Evie formations. In the areas where the microseismic data were obtained, gas is extracted from the formations along 10 horizontal wells which were hydraulically stimulated using a "zipper-frac" technique, where adjacent wells are fractured one after the other starting at the toes of the wells and working toward the heels (Figure 2). Events were recorded using 96 three-component geophones in three downhole arrays located near the heels of the treatment wells, with instruments primarily located within the Fort Simpson shales, a thick clay-rich organic-lean sequence that overlies the Horn River formation.

Over 92,000 events were recorded during 119 individual fracture stages carried out over a 17 day period. The events were detected and located by the contractor, ESG solutions, using a 1-D anisotropic velocity model (Figure S1 in the supporting information). This model was derived initially using sonic logs and calibrated using perforation shots with known time and position under the assumption of elliptical anisotropy (i.e., $\varepsilon = \delta$). It is notable that while many of the target reservoir layers are anisotropic, the strongest anisotropy is observed in the overlying Fort Simpson formation, which dominates the raypaths between the sources and the receivers.

3. Shear Wave Splitting

The data were analyzed using an automated splitting approach which allows for the easy processing of large data sets (Wuestefeld et al., 2010). For each source-receiver pair with an *S* pick, the seismogram is first rotated into the ray frame, to maximize the *S* energy on the transverse components. The two splitting parameters, δt and ψ, are then estimated using two different approaches: the cross-correlation technique and the eigenvalue method. The difference in the estimated parameters provided by these two methods is then used to produce an objective quality control in the form of a quality index which varies from −1.0 for null measurements to 0.0 for poor and +1.0 for good measurements. The ideal "good" measurement are characterized by identical splitting parameters from each method. Figure 3 shows a diagnostic plot from an example splitting measurements; note that the best splitting parameters are those that best linearize particle motion once a correction is made.

Splitting analyses were applied to all source-receiver pairs with an *S* pick resulting in ∼1.6 million measurements, of which ∼27,000 were considered high quality. We define a high-quality measurement as having a quality index greater than 0.85, an error in δt less than 5 ms, an error in ψ less than 10° and a signal-to-noise ratio greater than 6. Following estimation of the splitting parameters, δt is normalized by path length to express anisotropy as a percentage difference between the fast and slow *S* velocities, δV_S. The average uncertainty in event locations is estimated by the contractor to be around ±15 m. With most source-receiver path lengths exceeding 300 m this translates to an expected relative error in δV_S of around 5% due to event location uncertainty.

Figure 4a shows all the high-quality measurements plotted on an upper hemisphere projection. It is clear that the anisotropy is very strong, with δV_S exceeding 30% in some instances. The anisotropy is dominantly VTI since most fast directions are either *SH* (circumferential tick marks) or *SV* (radial tick marks) and the data are nearly symmetrical about the vertical axis. There also appears to be a transition from *SH* fast for horizontally propagating waves to *SV* fast for steeply propagating waves, indicating that the anisotropy cannot be elliptical. Although VTI dominates there is evidence of an overprinting HTI component, which is more clearly seen when the data are smoothed (Figure 4b). Notably, there is an azimuthal variation in the inclination of the *SV*-*SH* crossover (i.e., the line of zero *S* wave splitting, where the two *S* velocity surfaces cross) with long

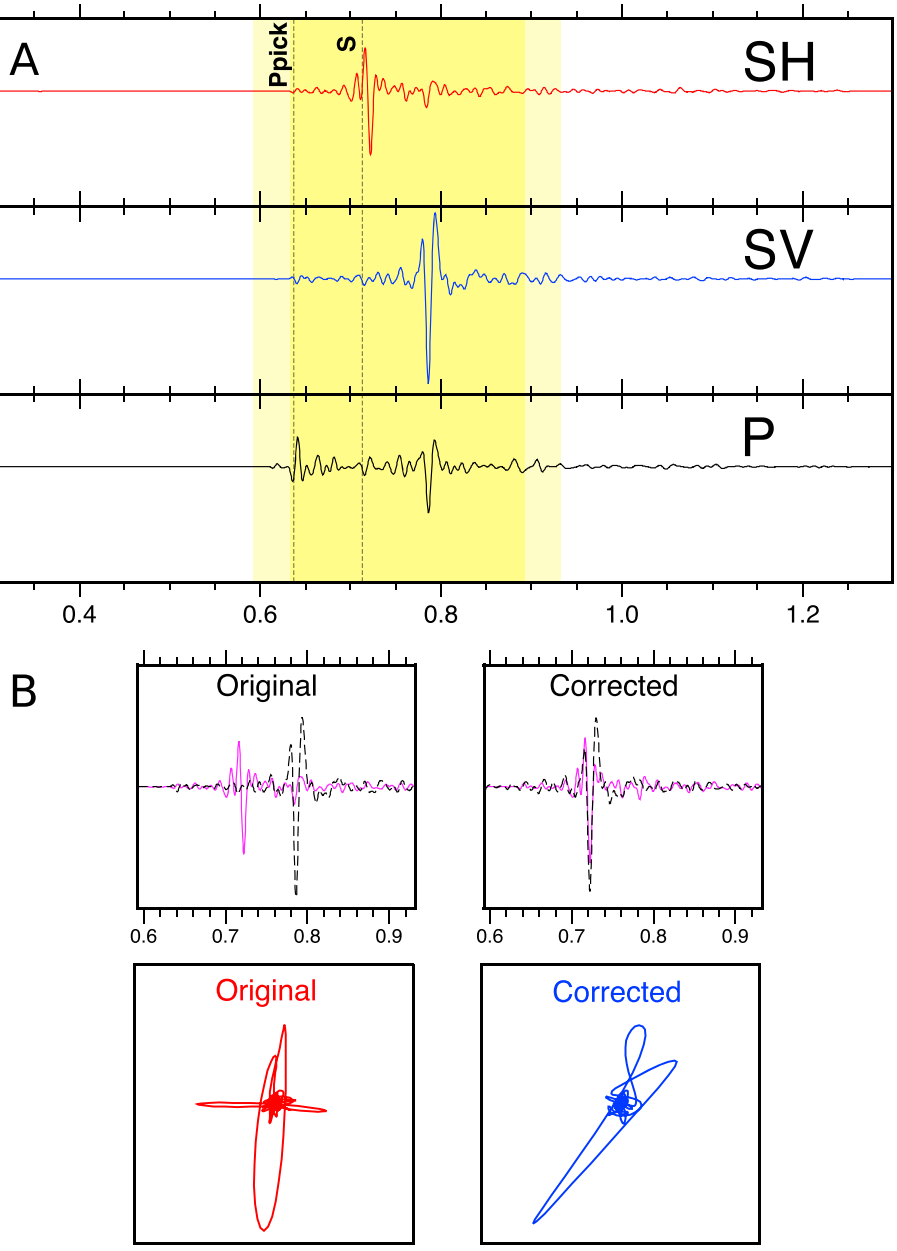

Figure 3. Diagnostic plot for an example splitting measurement. (a) The *SH*, *SV*, and *P* components of the seismogram and the time windows for splitting analysis. (b) *S* waveforms (top) and particle motions in the *SH-SV* plane (bottom) before and after the splitting correction is applied.

axis oriented NE-SW. Additionally, the magnitude of the background VTI anisotropy for near horizontal rays is reduced in this direction. These are both characteristic features of a vertical aligned fracture set embedded in a strongly anisotropic VTI background rock, suggesting a NE striking dominant vertical fracture set, roughly parallel to the regional horizontal compressive stress direction (Bell, 2015).

Since VTI dominates the anisotropy, we can visualize the *S* wave splitting as a function of inclination. Figure 5a shows how the magnitude of splitting varies with inclination for a subset of the measurements, chosen to minimize scatter due to azimuthal variations and lateral heterogeneity, with a color representing the polarization of the fast wave in the ray frame (blue for *SV*; red for *SH*). We can compare this to the predicted *S* wave splitting for anisotropic models defined by Thomsen parameters. The 1-D anisotropic velocity model used to locate the events provided estimates of ε and γ for each of the layers, but not for δ. For this analysis we will focus on the Fort Simpson shale, which is the thickest and most strongly anisotropic layer of the model, and,

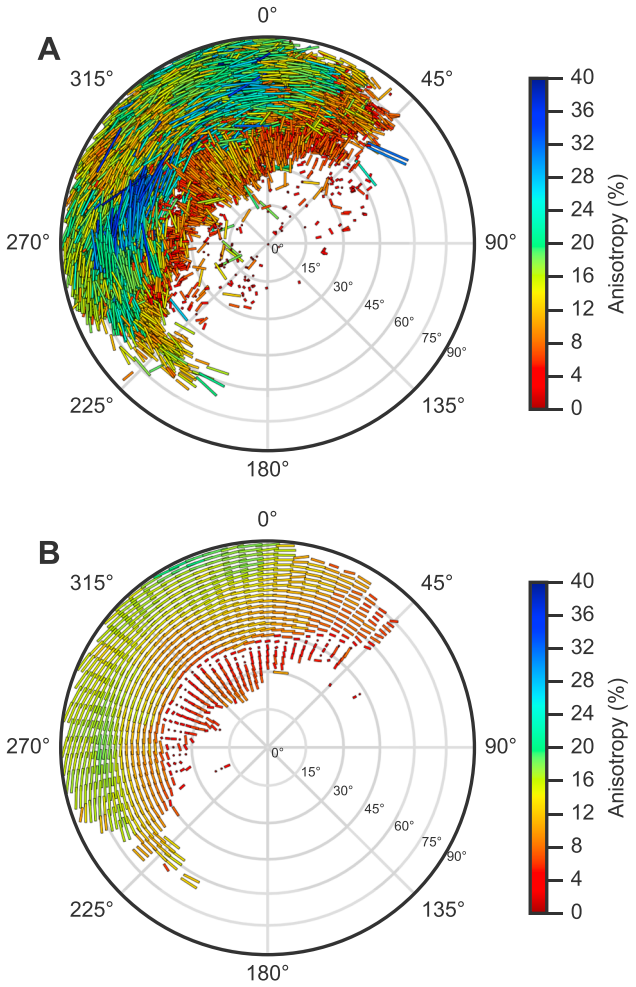

Figure 4. (a) Upper hemisphere plot showing all *S* wave splitting measurements. Tick mark location indicates ray azimuth and inclination, tick orientations indicate fast polarization direction, and tick length and color indicate the magnitude of the anisotropy. (b) Same as in Figure 4a but with measurements averaged within 5° × 5° bins.

due to the array geometry, dominates the splitting along most ray paths. Figure 5b shows the predicted *S*-wave splitting from the Fort Simpson shale, using the assumption of elliptical anisotropy (i.e., $\varepsilon = \delta$). This model does a reasonable job matching the splitting at high inclinations, however, a consequence of the assumption of elliptical anisotropy is that the predicted *SH* velocity is greater than or equal to the *SV* velocity for all inclinations, meaning that it fails to produce *SV-SH* crossover observed in the data.

If we assume ε and γ are reasonably well constrained in the velocity model we can attempt to get a better fit the observations simply by modifying the δ parameter. If δ is decreased from 0.36 to 0.15 (Figure 5c), we see a *SV-SH* crossover inclination that is reasonably close to observations (although with lower magnitudes at steep inclinations than observed), while maintaining the high-magnitude splitting for the near horizontal rays. Lowering δ further down to 0.0 better matches the magnitudes (Figure 5d) and produces an interesting feature where the *SV* wavefront folds over itself in the vicinity of 40° inclinations, resulting in traveltime triplications. Thus, observations of triplications in the waveforms can provide additional constraints on the relative magnitudes of δ and ε.

4. Observations of Shear Wave Triplications and Revision of Velocity Model

Shear wave triplications cannot be detected from SWS measurements alone. Instead, a manual inspection of the waveforms is required to confirm the effect, ideally over an array of geophones spanning the range of inclinations of the expected triplication, which is generally centered around 45°. Figure 6a shows an example of waveforms which appear to exhibit triplication in the *SV* phase between inclinations of around 35 and 55°. To confirm this is truly a triplication and to improve the anisotropic velocity model, we compare the waveforms to synthetic seismograms created using Maslov asymptotic theory (Guest & Kendall, 1993; Kendall & Thomson, 1993). Maslov asymptotic theory is an extension to ray theory, which, in addition to Fermat or geometric rays connecting the source and receiver, also considers neighboring non-Fermat rays. A result of this is that it provides valid waveforms in some regions where classical ray theory breaks down, such as in the vicinity of caustics where rays focus and waveforms fold back on themselves.

The model for the synthetics is composed of three layers above the source: the upper portion of the Otter Park formation, the Muskwa formation, and the Fort Simpson shales. Although the upper 13 receivers are located in layers above Fort Simpson, these layers are neglected from the synthetic model as the triplication is observed primarily on the lower 23 receivers. For the initial model we assumed that the vertical *P* and *S* velocities and Thomsen's ε and γ from the velocity model were correct (Figure S1) and simply reduced δ to 0.1 for the Muskwa and Otter Park layers following estimates of Sayers et al. (2015), and 0.0 for the Fort Simpson shale. We found that the model provided a reasonably good match for *SV*, reproducing a triplication similar to that observed; however, the traveltimes for *P* and *SH* did not match. In particular, the *P* to *S* separation time in the synthetics was smaller than observations for low (steep) inclinations suggesting further refinement of the velocity model was necessary.

The velocity model used for event location was calibrated under the assumption of elliptical anisotropy; however, the presence of triplications in the data indicates that the true anisotropy is highly anelliptical. Due to this inappropriate assumption, it is likely that the vertical velocities, and possibly the values of ε and γ, would need to deviate from their true values during the calibration in order to minimize traveltime misfits. To test this, we compared the vertical *P* and *S* velocities of the Fort Simpson shale from the velocity model to velocities measured from sonic logs in a near-vertical well (Figure S2a). We found that in order to better

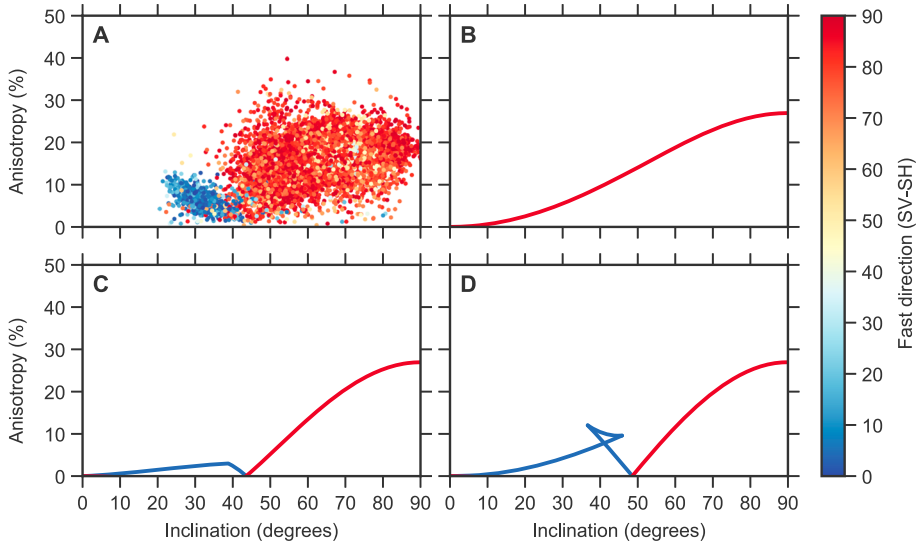

Figure 5. (a) *S* wave splitting for a subset of the data set versus raypath inclination. Predicted *S* wave splitting in the Fort Simpson shale assuming (b) elliptical anisotropy ($\delta = \varepsilon = 0.37$, $\sigma/\sigma_{crit} = 0$), (c) δ lowered to 0.15 producing a *SV-SH* crossover ($\sigma/\sigma_{crit} = 0.99$), and (d) δ lowered to 0.0 producing a triplication of *SV* ($\sigma/\sigma_{crit} = 1.66$). Color represents the polarization of the fast wave in the ray frame (*SV* blue; *SH* red).

match the sonic logs, we needed to revise the velocity model by increasing V_{P0} and decreasing V_{S0}. To update the associated Thomsen parameters, we compared the group velocities predicted with the original elliptical model to that of our revised anelliptical model (Figure S2) and adjusted the ε and δ parameters to minimize the difference in V_P between the models over the full range of inclinations while maintaining a triplication in *SV* of the appropriate size. The γ parameter was increased such that the horizontal *SH* velocity was similar to that in the elliptical model. Note that the first *S* arrival for each model matches reasonably well over all inclinations albeit with the revised model flipping between *SH* and *SV*. Details of the anisotropic parameters of both the initial and revised models are given in Table 1.

Figure 6 shows the observed *SV* waveforms along the corresponding synthetic waveforms and raypaths. The raypaths clearly show the ray focusing effect of the *SV* triplications, although it is notable the effect of triplications extend beyond the three receivers suggested by the raypaths, due to diffractions extending from the cusps of the triplication. We note that in addition to reproducing the triplications, the traveltimes of the *P* and *SH* phases also show good agreement with observations over the full range of inclinations (Figure S3).

5. Causes of VTI Anisotropy

To this point we have focused on estimating the magnitude of the VTI anisotropy of the overburden, without consideration of its causes. The primary factors that can contribute to seismic anisotropy in sedimentary rock

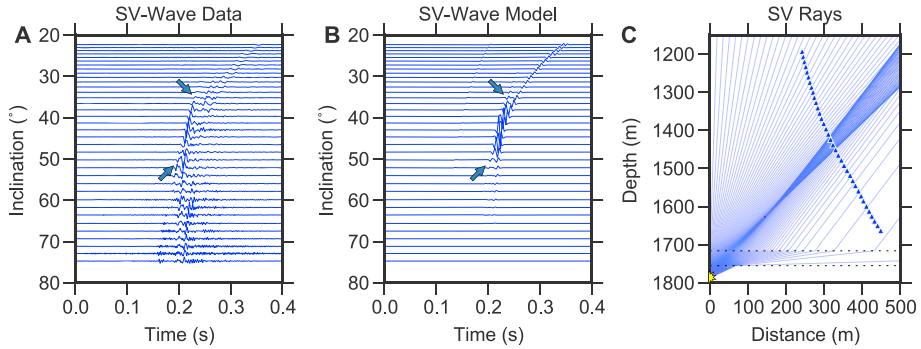

Figure 6. An example of *SV* waveforms exhibiting triplication from a microseismic event showing (a) raw waveforms, (b) synthetic waveforms, and (c) modeled raypaths. Traces are sorted by geometric inclination assuming a straight line path from source to receiver. Arrows indicate the cusps of the triplications.

Table 1
Estimated Velocity and Anisotropy Parameters of the Fort Simpson Shale From the Initial Elliptical Anisotropy Velocity Model and the Revised Anelliptical Model

Model	V_{P0} (km/s)	V_{S0} (km/s)	ε	γ	δ	σ/σ_{crit}
Initial	3.235	1.770	0.37	0.36	0.37	0.00
Revised	3.380	1.650	0.33	0.46	0.01	1.79

are the intrinsic anisotropy due to lattice-preferred orientation (LPO) of anisotropic minerals (e.g., Valcke et al., 2006; Vernik & Liu, 1997) and extrinsic anisotropy due to aligned fractures, cracks, pores, and grain boundary contacts, along with their infilling material (e.g., Allan et al., 2016; Kendall et al., 2007; Sayers, 2005).

5.1. Effect of Mineral Alignment

Figure 7 shows estimates of the modal fraction of minerals along one of the boreholes derived from X-ray fluorescence data as it passes from the Fort Simpson into the Muskwa formation, a contact which is marked by a sharp decrease in anisotropy parameters (both ε and γ, Figure S1b). The dominant mineral constituents are quartz and clays (illite, chlorite, and kaolinite) with some carbonates also present in the Muskwa. A notable observation is that the strongly anisotropic Fort Simpson Shale has a much larger proportion of clays than the more quartz-rich Muskwa ($\sim$ 60% versus $\sim$ 20–40%). This is consistent with observations that anisotropy of shales is often correlated with the amount of clay (e.g., Sone & Zoback, 2013). This is because clays and other phyllosilicate minerals have significant intrinsic anisotropy and often have strong LPO due to their platy nature (Sayers, 2005; Vernik & Liu, 1997), whereas quartz rarely has sufficient LPO to make a significant impact on aggregate anisotropy (Valcke et al., 2006).

The contribution of anisotropy due to LPO can be estimated by averaging single-crystal elastic constants based on their modal fraction and their crystal Orientation Distribution Functions (ODFs) (e.g., Kendall et al., 2007; Valcke et al., 2006). To do this, we first consider a small domain of shale within which all the clay platelets are aligned, and the remaining minerals (primarily quartz) are randomly oriented. Using the relative proportions of minerals, we can calculate the effective anisotropic elastic tensor of the domain by combining the single-crystal elastic constants of illite, chlorite, and kaolinite from Katahara (1996) with an isotropic quartz background using Voigt-Reuss-Hill averaging. For the Fort Simpson shale based on Figure 7, we consider a rock aggregate composed of 40% quartz, 36% illite, 16% kaolinite, and 8% chlorite. We can then introduce disorder in the alignment of these domains by averaging over an appropriate ODF.

Although we do not have petrofabric data to estimate the ODF of the clays directly, we can model the effect of clay alignment over a range of plausible textures using the theory of Sayers (1994, 2005), and the simplified matrix equations of Johansen et al. (2004). The theory assumes that both the local shale domains and the resulting ODF are transversely isotropic, which allows the ODF to be characterized with two expansion coefficients of generalized Legendre functions: W_{200} and W_{400}. The ODF or texture of the clay platelets are defined by their location within the (W_{200}, W_{400}) plane. The case of $W_{200} = W_{400} = 0$ corresponds to randomly oriented clay platelets producing an isotropic shale. At the other extreme when the clays are perfectly aligned, W_{200} and W_{400} take their maximum values ($W_{200}^{max} = \sqrt{10}/8\pi^2$ and $W_{400}^{max} = 3\sqrt{2}/8\pi^2$) resulting in very strong anisotropy. The effective anisotropic stiffness tensor is calculated using the Voigt approximation, from which the resulting Thomsen parameters can be determined.

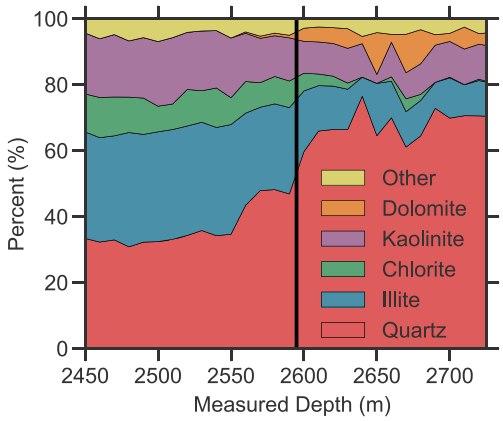

Figure 7. Variation in mineralogy, as inferred from X-ray florescence data, along a borehole as it crosses from the (left) Fort Simpson shale to the (right) Muskwa formation.

Although all combinations of W_{200} and W_{400} up to their maximum values are theoretically possible, in practice, disorder in clay platelet orientation tends to reduce W_{400} faster than W_{200} since W_{400} is a higher-order moment of the ODF (Sayers, 2005). Therefore, we would expect that the texture of natural shales would fall within the region of the (W_{200}, W_{400}) plane defined by $W_{400}/W_{200} \leq W_{400}^{max}/W_{200}^{max}$.

In Figure 8a we follow the approach of Pervukhina and Rasolofosaon (2015, 2017) and plot the range of possible anisotropies (ε and γ) for all possible values of W_{200} and W_{400}. The green line corresponds to textures for which $W_{400}/W_{200} = W_{400}^{max}/W_{200}^{max}$, meaning we would expect natural shale

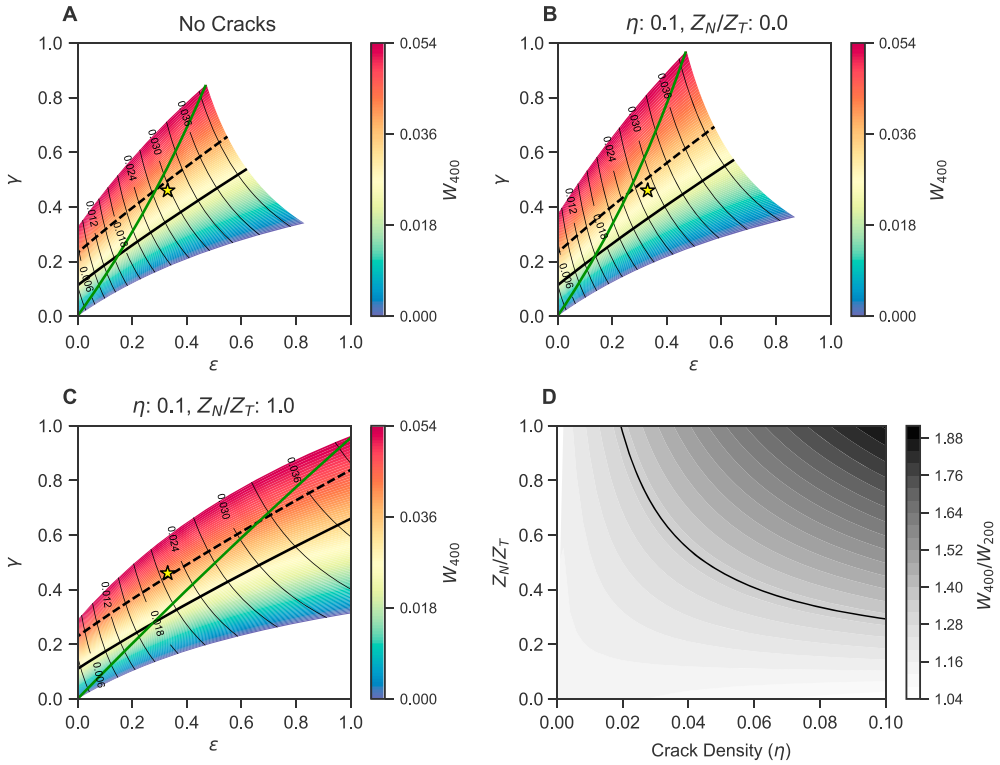

Figure 8. (a) Cross plot of Thomsen's ε versus γ for varying coefficients W_{400} (color) and W_{200} (thin isolines) of the ODF of clay platelets for a model composed of 60% clays (36% illite, 8% chlorite, and 16% kaolinite), and 40% quartz. Yellow star indicates the anisotropy of the Fort Simpson shale, and thick black line is isoline of incipient triplication (σ/σ_{crit} = 1.0); textures above this line will produce triplications and those below it will not. The dashed line indicates a triplication approximately of the size observed (σ/σ_{crit} = 1.79). Green line indicates textures where $W_{400}/W_{200} = W_{400}^{max}/W_{200}^{max}$; natural textures should plot below this line. (b) Same as in Figure 8a but for a model with additional cracks with crack density, η = 0.1 and Z_N/Z_T = 0.0, aligned with the same ODF as the clay platelets. (c) Same as Figure 8b but with Z_N/Z_T = 1.0; note that the resulting texture now plots above the green line. (d) Contour plot of W_{400}/W_{200} of the resulting textures for a range of crack parameters; solid line corresponds to $W_{400}/W_{200} = W_{400}^{max}/W_{200}^{max}$.

textures to fall below the line. In addition, we also plot isolines of σ/σ_{crit} values of 1 (solid line), corresponding to the line of incipient triplication separating triplicating textures above the line from nontriplicating textures below it, and 1.79 (dashed line) corresponding to the value for the best fitting model (Table 1).

The yellow star in Figure 8a indicates the anisotropy of the Fort Simpson shale (ε and γ) as inferred by the revised velocity model. We see that the corresponding clay platelet texture falls well within the triplicating field and predicts a triplication close to the size of that observed in the data, while satisfying the condition $W_{400}/W_{200} \leq W_{400}^{max}/W_{200}^{max}$ indicating it is a plausible texture. This suggests that the bulk of the anisotropy can be explained by the LPO of intrinsically anisotropic clay minerals; however, a more detailed analysis of the LPO would be required to test this.

5.2. Effect of Aligned Cracks or Grain Boundary Contacts

Although including the effect of aligned horizontal cracks are not strictly necessary to explain the observed anisotropy, it is expected that the compliance of contact regions between parallel aligned clay crystals should have some effect on the overall anisotropy (Sayers, 2005). Additionally, there is potentially also an effect of horizontal microcracks due to the thermal maturation of kerogen in laminated shale (Carcione & Avseth, 2015; Ougier-Simonin et al., 2016). To simulate this effect, we modified our rock physics model using the additional compliance approach of Schoenberg and Sayers (1995) to incorporate cracks defined by a crack density term (η, equivalent to the normalized crack density of Hall et al., 2008) and ratio of normal to tangential compliance (Z_N/Z_T), which we assume are oriented along the same ODF as the clay platelets (i.e., the orientation of the cracks is controlled by the texture of the clay minerals).

Figures 8b and 8c show examples of the predicted anisotropy for models incorporating cracks with a crack density of 0.1 and a Z_N/Z_T of 0.0 and 1.0, respectively. We see that for a low Z_N/Z_T the primary effect of increasing η for a fixed texture (i.e., a fixed point on the (W_{200}, W_{400}) plane) is to subtly increase γ but not ε, resulting in a relatively small change in anisotropy. In contrast, for the high Z_N/Z_T case adding cracks will increase both γ and, to a larger extent, ε. This makes sense intuitively because *P* wave velocities (and thus ε) are more sensitive to normal compliance (Z_N) than tangential compliance (Z_T).

A consequence of the enhanced anisotropy from the cracks is that different crack properties would require different textures to explain the observed values of γ and ε in the Fort Simpson shale (yellow stars in Figures 8a–8c). Interestingly, we find that the texture resulting from all crack-enhanced models produces a similar sized triplication (i.e., all models plot close to the dashed line corresponding to $\sigma/\sigma_{crit} = 1.79$); however, models with high values of Z_N/Z_T tend to require an increase in W_{400}/W_{200}, migrating to a texture outside the range that are likely to occur naturally (i.e., above the green line). This can be seen in Figure 8d which plots the values of W_{400}/W_{200} of the textures required for a range of crack parameters, with the black contour corresponding to $W_{400}^{max}/W_{200}^{max}$. We can clearly see from this that if cracks do contribute to the anisotropy, they must either have a low crack density or a low Z_N/Z_T in order to maintain a plausible texture.

6. Discussion and Conclusions

The results clearly demonstrate how the analysis of *S* wave splitting from microseismic sources combined with observations of triplications can help to improve anisotropic models. In particular, it provides constraints on the δ parameter, which is often difficult to measure accurately using core measurements (Dellinger & Vernik, 1994) but is one of the more important parameters for surface seismic exploration, as it controls the near-offset *P* wave anisotropy (Thomsen, 1986). Although, theoretically, the existence of shear wave triplications has been known for some time, we know of only a few examples of inferred or observed triplications in field data (Hake et al., 1998; Jolly, 1956; Slater et al., 1993). This is despite a recent statistical analysis of published anisotropy parameters which suggests that over 25% of shales should be expected to produce triplications (Horne, 2013). This may in part be due to the fact that the reflection angles of converted waves in typical surface seismic reflection experiments rarely extend to the inclinations where triplications would be expected. However, with the recent increase in downhole microseismic monitoring of hydraulic fracture stimulations, it is likely such triplications are recorded in many data sets but may be ignored due to lack of awareness. To our knowledge this is the first published example of a clear triplication due to anisotropy observed in microseismic data.

We have shown that by combining estimates of the modal proportions of minerals and their single-crystal intrinsic anisotropies, we can infer details of the texture of clay minerals in shale and estimate their likely contribution to the overall anisotropy. However, one of the limitations of our method is that we assume that all the clay minerals aligned to the same degree. In reality this is likely not the case. For example, Valcke et al. (2006) used X-ray Texture Goniometry to measure the LPO of phyllosilicates in a suite of sedimentary rocks from the North Sea. They found that detrital mica typically showed strong alignment, whereas authigenic clays such as chlorite and kaolinite were often fine grained and had a more diffuse ODF. Samples of the Fort Simpson shale were not available to directly determine the ODF of its mineral constituents. Such analysis would provide greater constraints on the texture of the various constituent minerals and further insight into the relative contribution of microcracks to the anisotropy.

Although at this stage we cannot conclusively say that horizontal microcracks are providing a significant contribution to the VTI anisotropy, we can say that if they do contribute then the cracks would need to have a relatively low Z_N/Z_T. A low Z_N/Z_T is typical of fluid-filled cracks with low hydraulic connectivity (e.g., Chapman, 2003; Hudson et al., 1996; Pointer et al., 2000), which would be expected for a low-permeability shale. Recent investigations into temporal changes in anisotropy during hydraulic stimulation have suggested that the Z_N/Z_T of fractures can increase as a result of reactivation leading to increased fracture connectivity (Baird et al., 2013; Verdon & Wüstefeld, 2013). We do not see clear temporal variations in the Fort Simpson shale, however, as it is organically very lean and is not being actively stimulated but simply overlies the target units of the Horn River formation. Recent rock physics modeling and laboratory investigations suggests that bedding aligned cracks may have a stronger effect on the VTI anisotropy of thermally mature organic-rich shales (Allan et al., 2016; Carcione & Avseth, 2015). This is because the conversion of load-bearing kerogen in laminated shales to oil and gas effectively results in an increase in horizontally aligned pores. Indeed, we were provided with some rock samples from the Horn River Formation and SEM analysis revealed that horizontal microfrac-

tures are present (Figure S4). These fractures appear to have formed as a result of organic matter maturation and filled with bitumen, which itself thermally matured and exsolved gas resulting in the formation of organic matter porosity. Identification of such fractures not only provide weaknesses that could be reactivated during hydraulic fracturing to provide conduits for gas flow but they also provide some evidence that horizontal fractures could exist in the overburden. Although hydraulic stimulations are often thought to be dominated by the creation and reactivation of steeply dipping fractures, experimental studies have shown that deformation on these macrofractures can induce microfractures to develop which tend to localize along grain boundaries or regions of contrasting mechanical properties controlled by the fabric, sometimes connecting previously isolated pores of organic material (e.g., Daigle et al., 2017). Additionally, recent investigations into the moment tensors of microseismic events during stimulation have highlighted the importance of bedding parallel slip (Rutledge et al., 2015; Urbancic et al., 2016). This suggests that horizontal microcracks, which may contribute to the VTI anisotropy of the rock, could interact with induced hydraulic fractures as a mechanism to facilitate gas flow. The methodology described here provides a means of monitoring the evolution of horizontal fractures during stimulation using microseismic sources. The requires surveys with sufficient ray coverage to characterize the two shear waves that propagate in an anisotropic medium, including any shear wave triplications. In field settings, this is only really feasible with downhole seismic monitoring arrays, but we note that it could be also applied to vertical-seismic-profiling (VSP) or cross-borehole surveys with active *S* wave sources. Furthermore, our approach is equally applicable in laboratory rock testing using ultrasonic *S* wave sources or acoustic emissions experiments.

Acknowledgments
We are grateful to Nexen for providing the data and allowing us to publish the results. We would like to thank Associate Editor Martha Savage for handling the manuscript, which benefitted from the constructive reviews of Sarah Brownlee and an anonymous reviewer. Funding for the work was provided by the sponsors of the Bristol University Microseismicity Projects (BUMPS, https://www1.gly.bris.ac.uk/BUMPS/), the sponsors of FRACGAS (http://www.see.leeds.ac.uk/research/igt/research-projects/fracgas/), and by the NERC grant NE/L008351/1. The shear wave splitting data for this paper are available in the supporting information section as a csv file.

References

Allan, A. M., Clark, A. C., Vanorio, T., Kanitpanyacharoen, W., & Wenk, H.-R. (2016). On the evolution of the elastic properties of organic-rich shale upon pyrolysis-induced thermal maturation. *Geophysics*, *81*(3), D263–D281.

Baird, A. F., Kendall, J.-M., Verdon, J. P., Wuestefeld, A., Noble, T. E., Li, Y., … Fisher, Q. J. (2013). Monitoring increases in fracture connectivity during hydraulic stimulations from temporal variations in shear wave splitting polarization. *Geophysical Journal International*, *195*(2), 1120–1131. https://doi.org/10.1093/gji/ggt274

Bell, J. S. (2015). In situ stress orientations and magnitudes in the Liard basin of western Canada (Tech. Rep. Open File 7049) (410 pp.). Ottawa, ON, Canada: Geological Survey of Canada. https://doi.org/10.4095/295742

Carcione, J. M., & Avseth, P. (2015). Rock-physics templates for clay-rich source rocks. *Geophysics*, *80*(5), D481–D500.

Chapman, M. (2003). Frequency-dependent anisotropy due to meso-scale fractures in the presence of equant porosity. *Geophysical Prospecting*, *51*(5), 369–379.

Crampin, S. (1984). Effective anisotropic elastic constants for wave propagation through cracked solids. *Geophysical Journal of the Royal Astronomical Society*, *76*(1), 135–145.

Daigle, H., Hayman, N. W., Kelly, E. D., Milliken, K. L., & Jiang, H. (2017). Fracture capture of organic pores in shales. *Geophysical Research Letters*, *44*, 2167–2176. https://doi.org/10.1002/2016GL072165

Dellinger, J., & Vernik, L. (1994). Do traveltimes in pulse-transmission experiments yield anisotropic group or phase velocities? *Geophysics*, *59*(11), 1774–1779.

Dellinger, J. A. (1991). Anisotropic seismic wave propagation (PhD thesis). Stanford University.

Guest, W. S., & Kendall, J.-M. (1993). Modelling seismic waveforms in anisotropic inhomogeneous media using ray and Maslov asymptotic theory: Applications to exploration seismology. *Journal of Exploration Geophysics*, *29*, 78–92.

Hake, J. H., Gevers, E. C. A., Van Der Kolk, C. M., & Tichelaar, B. W. (1998). A shear experiment over the Natih field in Oman: Pilot seismic and borehole data. *Geophysical prospecting*, *46*(6), 617–646.

Hall, S. A., & Kendall, J.-M. (2003). Fracture characterization at Valhall: Application of *P*-wave amplitude variation with offset and azimuth (AVOA) analysis to a 3D ocean-bottom data set. *Geophysics*, *68*, 1150–1160.

Hall, S. A., Kendall, J.-M., Maddock, J., & Fisher, Q. (2008). Crack density tensor inversion for analysis of changes in rock frame architecture. *Geophysical Journal International*, *173*(2), 577–592.

Horne, S. A. (2013). A statistical review of mudrock elastic anisotropy. *Geophysical Prospecting*, *61*(4), 817–826.

Hudson, J. A. (1980). Overall properties of a cracked solid. *Mathematical Proceedings of the Cambridge Philosophical Society*, *88*(2), 371–384.

Hudson, J. A., Liu, E., & Crampin, S. (1996). The mechanical properties of materials with interconnected cracks and pores. *Geophysical Journal International*, *124*(1), 105–112.

Johansen, T. A., Ole Ruud, B., & Jakobsen, M. (2004). Effect of grain scale alignment on seismic anisotropy and reflectivity of shales. *Geophysical Prospecting*, *52*(2), 133–149.

Jolly, R. N. (1956). Investigation of shear waves. *Geophysics*, *21*(4), 905–938.

Katahara, K. W. (1996). Clay mineral elastic properties. In *1996 SEG Annual Meeting*. Denver, CO: Society of Exploration Geophysicists.

Kendall, J.-M., & Thomson, C. J. (1993). Maslov ray summation, pseudo-caustics, Lagrangian equivalence and transient seismic waveforms. *Geophysical Journal International*, *113*(1), 186–214.

Kendall, J.-M., Fisher, Q. J., Covey Crump, S., Maddock, J., Carter, A., Hall, S. A., … Ben Ismail, W. (2007). Seismic anisotropy as an indicator of reservoir quality in siliciclastic rocks. *Geological Society, London Special Publications*, *292*(1), 123–136.

Lynn, H. B., & Thomsen, L. A. (1990). Reflection shear-wave data collected near the principal axes of azimuthal anisotropy. *Geophysics*, *55*(2), 147–156.

Ougier-Simonin, A., Renard, F., Boehm, C., & Vidal-Gilbert, S. (2016). Microfracturing and microporosity in shales. *Earth-Science Reviews*, *162*, 198–226.

Pervukhina, M., & Rasolofosaon, P. N. J. (2015). Burial/compaction and seismic anisotropy in shaly formations. In *77th EAGE Conference and Exhibition 2015*. Madrid, Spain.

Pervukhina, M., & Rasolofosaon, P. N. J. (2017). Compaction trend versus seismic anisotropy in shaly formations. *Geophysical Prospecting*, *65*(5), 1351–1365.

Pointer, T., Liu, E., & Hudson, J. A. (2000). Seismic wave propagation in cracked porous media. *Geophysical Journal International*, *142*(1), 199–231.

Rutledge, J., Yu, X., & Leaney, S. (2015). Microseismic shearing driven by hydraulic-fracture opening: An interpretation of source-mechanism trends. *The Leading Edge*, *34*(8), 926–934.

Sayers, C., den Boer, L., Dasgupta, S., & Goodway, B. (2015). Anisotropy estimate for the Horn River Basin from sonic logs in vertical and deviated wells. *The Leading Edge*, *34*(3), 296–306.

Sayers, C. M. (1994). The elastic anisotropy of shales. *Journal of Geophysical Research*, *99*(B1), 767–774.

Sayers, C. M. (2005). Seismic anisotropy of shales. *Geophysical Prospecting*, *53*(5), 667–676.

Schoenberg, M., & Sayers, C. M. (1995). Seismic anisotropy of fractured rock. *Geophysics*, *60*, 204–211.

Slater, C., Crampin, S., Brodov, L. Y., & Kuznetsov, V. M. (1993). Observations of anisotropic cusps in transversely isotropic clay. *Canadian Journal of Exploration Geophysics*, *29*(1), 216–226.

Sone, H., & Zoback, M. D. (2013). Mechanical properties of shale-gas reservoir rocks—Part 1: Static and dynamic elastic properties and anisotropy. *Geophysics*, *78*(5), D381–D392.

Thomsen, L. (1986). Weak elastic anisotropy. *Geophysics*, *51*(10), 1954–1966.

Thomsen, L., & Dellinger, J. (2003). On shear-wave triplication in transversely isotropic media. *Journal of Applied Geophysics*, *54*(3), 289–296.

Tsvankin, I., & Thomsen, L. (1994). Nonhyperbolic reflection moveout in anisotropic media. *Geophysics*, *59*(8), 1290–1304.

Urbancic, T. I., Baig, A., & Viegas Fernandes, G. (2016). The role of pre-existing fractures in constraining stimulations in the reservoir. In *78th EAGE Conference and Exhibition*.

Valcke, S. L. A., Casey, M., Lloyd, G. E., Kendall, J.-M., & Fisher, Q. J. (2006). Lattice preferred orientation and seismic anisotropy in sedimentary rocks. *Geophysical Journal International*, *166*(2), 652–666.

van der Baan, M., & Kendall, J.-M. (2002). Estimating anisotropy parameters and traveltimes in the τ-p domain. *Geophysics*, *67*(4), 1076–1086.

Verdon, J. P., & Wüstefeld, A. (2013). Measurement of the normal/tangential fracture compliance ratio (Z_N/Z_T) during hydraulic fracture stimulation using S-wave splitting data. *Geophysical Prospecting*, *61*, 461–475. https://doi.org/10.1111/j.1365-2478.2012.01132.x

Verdon, J. P., Kendall, J.-M., & Wüstefeld, A. (2009). Imaging fractures and sedimentary fabrics using shear wave splitting measurements made on passive seismic data. *Geophysical Journal International*, *179*(2), 1245–1254. https://doi.org/10.1111/j.1365-246X.2009.04347.x

Vernik, L., & Liu, X. (1997). Velocity anisotropy in shales: A petrophysical study. *Geophysics*, *62*(2), 521–532.

Vernik, L., & Nur, A. (1992). Ultrasonic velocity and anisotropy of hydrocarbon source rocks. *Geophysics*, *57*(5), 727–735.

Wuestefeld, A., Al-Harrasi, O., Verdon, J. P., Wookey, J., & Kendall, J.-M. (2010). A strategy for automated analysis of passive microseismic data to image seismic anisotropy and fracture characteristics. *Geophysical Prospecting*, *58*(5), 755–773.